Supermassive Black Hole Property Determination via Gravitational Radiation from Eccentrically Orbiting Stellar Mass Black Hole Binaries: Final Report

Andrew Laeuger, Brian Seymour, Yanbei Chen, Hang Yu

(Dated: April 2022)

The gravitational waveform from a compact inspiraling binary, such as a binary black hole (BBH), can indicate the presence of a nearby massive body, such as a supermassive black hole (SMBH). The waveform is modulated by de Sitter precession of the BBH's inner angular momentum and by the time-dependent Doppler phase shift of the BBH in its orbit. The future generation of space-based GW observatories, focused on the millihertz and decihertz band, is uniquely poised to observe these waveform modulations, as the GW frequency from stellar-mass BBHs remains in this band for the months or years over which these modulation effects accumulate. In this work, we apply the Fisher information matrix to estimate how well low-frequency GW detectors can measure properties of BBH+SMBH hierarchical triples. We consider an eccentric orbit of the BBH about the SMBH, extending previous studies which were limited to circular orbits. We find that the uncertainties in measurements of the SMBH mass and semimajor axis can be improved by a factor of a few when the BBH takes a non-circular orbit and that decihertz detector concepts like TianGO enable better sensitivity than proposed detectors at even lower frequencies, like LISA. Furthermore, the eccentricity, outer orbital angular frequency, and outer orbit initial phase and argument of pericenter are very well measured.

I. BACKGROUND AND OBJECTIVES

Since the first detection of gravitational waves (GWs) by LIGO in 2015, GW astronomy has cemented itself as a legitimate and advantageous method for observing binary systems of compact objects, the majority of which are binary black holes (BBHs) [1–3]. Currently, the ground detectors in LIGO/Virgo/KAGRA are most sensitive between 10 Hz to a few kHz, which describes the final moments before merger. In order for a GW detector to be sensitive to frequencies below 1 Hz, it must be built in space, where forming an interferometer with arm lengths much greater than LIGO's is feasible. LISA is a planned space based detector which would specialize in the millihertz band $\sim 10^{-3} - 10^{-1}$ Hz [4].

There are detector concepts which lie in the decihertz range – between LISA and ground-based detectors – such as B-DECIGO [5] and TianGO [6, 7], which may expand the range of astrophysical systems we can observe via GWs. These space-borne GW observatories could monitor inspiraling compact binary systems at times long before their orbital frequencies climb into the frequency bands of active ground-based detectors. Furthermore, since the instantaneous orbital decay timescale due to GW emission scales as $\tau_{GW} \propto \omega_{orb}^{-8/3}$ [8], a stellar-mass BBH system will remain in the frequency band of these low-frequency observatories much longer than in the frequency band of ground-based experiments. This will allow space-based observatories to monitor properties of a BBH system which may change over time scales on the order of years.

Consider a stellar-mass BBH orbiting around a supermassive black hole (SMBH), as depicted in Figure 1 along with the orientation of a hypothetical space-based GW detector orbiting the Sun. It is well known that the presence of the SMBH induces coupling between the outer orbit (the BBH orbiting the SMBH) and the inner orbit (the two stellar-mass BHs in the binary) which modulates the gravitational waves emitted by the inspiraling BBH. For example, the orbital angular momentum of the inner binary $\hat{L}_i$ experiences de Sitter precession about the orbital angular momentum of the outer binary $\hat{L}_o$, and the progression of the BBH in its orbit about the SMBH produces a Doppler shift in the GWs it radiates [9] (see Section II for explicit expressions). The Lidov-Kozai effect also plays a role in the evolution of hierarchical triples, though in this work, its effect on the waveform is neglected (see Section II C for discussion).

We can measure triple system properties such as SMBH mass, semimajor axis of the outer orbit, and other geometrical angles from the effects of de Sitter precession and of Doppler shifts on the waveform. In a recent work by Yu and Chen, it is shown that this probe can feasibly measure properties of interest to the few percent level over a wide range of possible BBH+SMBH systems [10]. Current observational methods for measuring properties of SMBHs and their local environments include tracking the orbital dynamics of nearby test masses, like stars, and reverberation mapping of the emission line fluxes from the accretion disk, if the SMBH is active [11]. Adding this technique to such a toolkit could expand the set of observable SMBHs with well-constrained properties to those which may have few electromagnetic radiation sources nearby [10].

The initial work of Yu and Chen assumes a perfectly circular outer orbit in the BBH+SMBH triple system; however, it is expected that formation channels for these systems, especially those which are dynamical in nature, should produce a sizeable population of triples with eccentric outer orbits [12]. As demonstrated in Section II, a nonzero eccentricity of the outer orbit leads to waveform modulation effects with larger magnitudes or time variance in comparison to the circular outer orbit scenario. In this work, we examine how the eccentricity of

θ^a	Definition
$\log \mathcal{M}_z$	Detector Frame Chirp Mass: $\mu^{3/5}(m_1 + m_2)^{2/5}$
q	Mass Ratio m_2/m_1
$\log D_L$	Luminosity Distance
t_c	Coalescence Time
ϕ_c	Coalescence Phase
$\bar{\theta}_S, \bar{\phi}_S$	Line of Sight of BBH+SMBH Triple
$\bar{\theta}_J, \bar{\phi}_J$	Orientation of Total Angular Momentum $\boldsymbol{J}$
λ_L	Angle Between $\boldsymbol{L}_i$ and $\boldsymbol{L}_o$
α_0	Initial Phase of $\boldsymbol{L}_i$ Around $\boldsymbol{L}_o$
$\log M_3$	SMBH Mass
$\log a_o$	Outer Orbit Semimajor Axis
γ_o	Outer Orbit Argument of pericenter
e_o	Outer Orbit Eccentricity
ϕ_o	Outer Orbit Initial Phase

TABLE I. Relevant parameters in BBH+SMBH triple system for GW observed by detectors. Bars over angles indicate the Solar System coordinate frame.
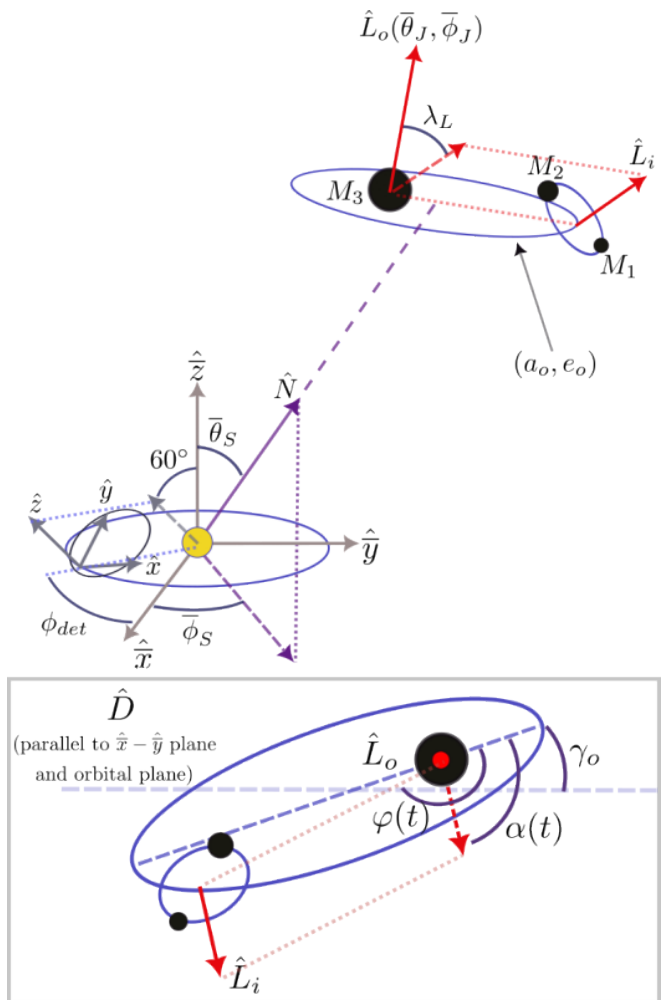

FIG. 1. Top: Geometry of the SMBH+BBH triple system. Bottom, inset: View of the triple system normal to the plane of the outer orbit. See the discussion below and Table I for definition of all parameters. Figure dimensions do not give any indication of true scale. In this work, we neglect the precession of γ_o as the BBH orbits the SMBH.

the outer orbit affects parameter measurement uncertainties. In order to estimate such uncertainties, we rely on the Fisher information matrix, a method which has been frequently used in the past to gauge the measurability of compact binary parameters by ground-based GW observatories [13].

In Section II, we outline the mathematical description of the gravitational waveform emitted from a BBH in a hierarchical triple and detected by a space-borne observatory. In Section III, we outline the Fisher matrix calculation as applied to parameter estimation and explain some simplifications we make to the computation. In Section IV, we present the results of our Fisher matrix computations, and in Section V, we offer conclusions and possible directions for this work to proceed in the future. In this work, we use geometrized units $G = c = 1$.

II. MATHEMATICAL DESCRIPTION OF THE SMBH+BBH TRIPLE SYSTEM

A. Geometry

We first describe the full geometry of the SMBH+BBH triple system with an eccentric outer orbit. Table I below outlines the set of relevant parameters used in calculating the waveform measured by a space-borne GW observatory. In Figure 1, the barred coordinates demarcate a Solar System centered coordinate system, while the unbarred coordinates demarcate a coordinate system based on the orientation of the observatory.

In order to compute the antenna response, we need to be able to convert from the unbarred coordinates to the barred coordinates, which is as follows:

$$\hat{x} = -\frac{1}{4}\sin(2\phi_d)\hat{\bar{x}} + \frac{3 + \cos(2\phi_d)}{4}\hat{\bar{y}} + \frac{\sqrt{3}}{2}\sin(\phi_d)\hat{\bar{z}} \quad (1)$$

$$\hat{y} = \frac{-3 + \cos(2\phi_d)}{4}\hat{\bar{x}} + \frac{1}{4}\sin(2\phi_d)\hat{\bar{y}} - \frac{\sqrt{3}}{2}\cos(\phi_d)\hat{\bar{z}} \quad (2)$$

$$\hat{z} = -\frac{\sqrt{3}}{2}\cos(\phi_d)\hat{\bar{x}} - \frac{\sqrt{3}}{2}\sin(\phi_d)\hat{\bar{y}} + \frac{1}{2}\hat{\bar{z}}. \quad (3)$$

The sky location of the hierarchical triple is $(\bar{\theta}_S, \bar{\phi}_S)$, which points along the vector $\hat{N}$, and has a luminosity distance of d_L. The triple itself consists of a BBH with black holes of masses M_1 and M_2, or equivalently, a chirp mass of $\mathcal{M} = \frac{(M_1 M_2)^{3/5}}{(M_1 + M_2)^{1/5}}$ and mass ratio of $q = M_2/M_1$, and an SMBH of mass M_3. The shape of the BBH's orbit around the SMBH can be determined entirely (at least to a sufficiently close approximation) by the semimajor

axis a_o and the eccentricity e_o.

The unit vector of the angular momentum of the two lighter black holes in the binary system is $\hat{L}_i$, and the unit vector of the angular momentum of the binary's orbit about the SMBH is $\hat{L}_o$. The opening angle λ_L is defined by

$$\cos \lambda_L = \hat{L}_o \cdot \hat{L}_i. \tag{4}$$

The opening angle stays constant in time, but the orientation of $\hat{L}_i$ traces a cone around $\hat{L}_o$ due to de Sitter precession, with

$$\frac{d\hat{L}_i}{dt} = \Omega_{dS}\hat{L}_o \times \hat{L}_i. \tag{5}$$

Using Eq. 9.200 of [14], we find the de Sitter precession frequency

$$\Omega_{dS}(t) = \frac{3}{2}\Omega_o \frac{M_3}{a_o(1-e_o^2)}\left[\frac{\left(1+e_o\cos(\varphi(t))\right)^3}{(1-e_o^2)^{3/2}}\right], \tag{6}$$

where $\Omega_o = \sqrt{M_3/a_o^3}$ and $\varphi(t)$ is the true orbital anomaly, the angle measured around the elliptical orbital path as centered on the focus of the ellipse occupied by the SMBH (as shown in the inset of Figure 1). The secular precession rate agrees with that in the introduction of [10]: that is, when integrated over one full orbital period of the BBH around the SMBH, the orbit-averaged de Sitter precession frequency that matches Eq. 1 of [10]. The phase of $\hat{L}_i$ in this cone, as shown in the inset of Figure 1, can be found by integrating the time-dependent de Sitter precession rate:

$$\alpha(t) = \alpha_0 + \int_t^{t_c} \Omega_{dS}(t')dt', \tag{7}$$

where α_0 is the phase at the time of the binary coalescence t_c.

Finally, to quantify the Doppler shift, we need to find a few additional parameters. First, the inclination of the outer orbit angular momentum follows

$$\cos \iota_J = \hat{N} \cdot \hat{L}_o. \tag{8}$$

Next, the argument of pericenter, γ_o, is defined as the angle between the major axis of the elliptical orbit and the line in space which is parallel to both the plane of the orbit *and* the $\hat{\tilde{x}} - \hat{\tilde{y}}$ plane. It is well known that an elliptical orbit does not admit an analytical solution for the position in the orbit as a function of time. However, there are some well-established numerical methods for solving this problem. The distance of the BBH from the SMBH is given by

$$r(t) = \frac{a_o(1-e_o^2)}{1+e_o\cos(\varphi(t))}, \tag{9}$$

with $\varphi(t)$ once again being the true orbital anomaly as in Figure 1. To find the true orbital anomaly, we must first find the eccentric anomaly, which is similar to the true orbital anomaly except that the origin used for this quantity is the center of the ellipse rather than the focus where the SMBH is located. Kepler's equation gives the relation between the eccentric anomaly u and time:

$$u(t) - e_o \sin(u(t)) = \left[\sqrt{\frac{M_3}{a_o^3}}t + \phi_o\right] \mod 2\pi$$
$$= \left[2\pi\frac{t}{P_o} + \phi_o\right] \mod 2\pi, \tag{10}$$

where ϕ_o is the phase of the outer orbit when $t = 0$. We then apply Newton's method to find $u(t)$, as this equation does not have an analytical solution. Explicitly, we conduct an iterative process, where $u_1 = 2\pi\frac{t}{P_o} + \phi_o$ and

$$u_{n+1} = u_n + \frac{u_1 - (u_n - e_o \sin u_n)}{1 - e_o \cos u_n}. \tag{11}$$

Usually, only roughly five iterations are needed to obtain high accuracy in $u(t)$. The eccentric anomaly can be converted to the orbital anomaly using

$$\tan(\frac{1}{2}\varphi(t)) = \sqrt{\frac{1+e_o}{1-e_o}}\tan(\frac{1}{2}u(t)). \tag{12}$$

B. Waveform

We can now proceed to calculate the strain detected by the space-based observatory, using the results of [9]. The overall measured signal is

$$h_{meas} = h_C\sqrt{(A_+F_+)^2 + (A_\times F_\times)^2}$$
$$\times \exp\{-i[\Phi_P + 2\Phi_T + \Phi_D]\}, \tag{13}$$

where h_C is the carrier waveform of the BBH, A and F are the polarization-dependent amplitude modulation and antenna response, respectively, and Φ_P, Φ_D, and Φ_T are the polarization, Thomas, and Doppler phases. It is this signal that we use to calculate elements of the Fisher information matrix. Post-Newtonian expansion gives a carrier waveform, in the frequency domain (and geometrized units $G = c = 1$), of

$$\tilde{h}_C(f_{GW}) = \left(\frac{5}{96}\right)^{1/2}\frac{\mathcal{M}^{5/6}}{\pi^{2/3}d_L}f_{GW}^{-7/6}$$
$$\times \exp\{i[2\pi f_{GW}t_c - \phi_c - \frac{\pi}{4} + \frac{3}{4}(8\pi\mathcal{M}f_{GW})^{-5/3}]\}, \tag{14}$$

where t_c and ϕ_c are the time and phase at coalescence. Roughly, the time corresponding to a given GW frequency follows:

$$t(f_{GW}) \approx t_c - \frac{5}{256\pi^{8/3}}\frac{1}{\mathcal{M}^{5/3}f_{GW}^{8/3}}. \tag{15}$$

The stationary phase approximation allows us to easily convert time-dependent waveform components, such as the evolution of the outer orbit, into frequency-dependent components that are applicable to the Fisher matrix formalism [15].

The two polarizations of the strain, h_+ and $h_\times$, are modified by the amplitude factors

$$A_+ = 1 + (\hat{L}_i \cdot \hat{N})^2 \tag{16}$$

$$A_\times = -2\hat{L}_i \cdot \hat{N}, \tag{17}$$

and furthermore, the detector response F for a 90-degree detector to incoming waves of each polarization varies, as

$$F_+(\theta_S, \phi_S, \psi_S) = \frac{1}{2}(1 + \cos^2\theta_S)\cos 2\phi_S \cos 2\psi_S \\ - \cos\theta_S \sin 2\phi_S \sin 2\psi_S \tag{18}$$

$$F_\times(\theta_S, \phi_S, \psi_S) = \frac{1}{2}(1 + \cos^2\theta_S)\cos 2\phi_S \sin 2\psi_S \\ + \cos\theta_S \sin 2\phi_S \cos 2\psi_S, \tag{19}$$

where

$$\tan\psi_S(t) = \frac{\hat{L}_i \cdot \hat{z} - (\hat{L}_i \cdot \hat{N})(\hat{z} \cdot \hat{N})}{\hat{N} \cdot (\hat{L}_i \times \hat{z})}. \tag{20}$$

Note the use of the detector-frame coordinates in Eq. 20. This detector response applied to a 60-degree detector such as LISA has a different form, and further still, the response F varies for each pair of arms in the triangular detector.

The first of the three additional phases is the polarization phase, which allows us to rewrite the signal strain in terms of a single amplitude and a modifying phase, seen in Eq. 13 (as opposed to $h(t) = h_+(t)F_+(t) + h_\times(t)F_\times(t)$). It is given by

$$\tan\Phi_P(t) = -\frac{A_\times(t)F_\times(t)}{A_+(t)F_+(t)}. \tag{21}$$

The second is the Thomas phase, which can be understood as the change in signal phase which results from ensuring that the orbital separation vector remains orthogonal to the angular momentum as the angular momentum precesses. It is given by

$$\Phi_T(t) = -\int_t^{t_c} dt \left[\frac{\hat{L}_i \cdot \hat{N}}{1 - (\hat{L}_i \cdot \hat{N})^2}\right](\hat{L}_i \times \hat{N}) \cdot \frac{d\hat{L}_i}{dt}, \tag{22}$$

The final phase term is the Doppler phase shift, the phase shift induced by the evolving distance between the detector and the GW source. There are two contributions to this phase. The first is the contribution from the detector, given at a particular time t by

$$\Phi_{D,det}(f_{GW}) = 2\pi f_{GW}(1 \text{ AU})\sin\theta_S \cos(\phi_{det} - \phi_S), \tag{23}$$

The other is from the source, which is modulated by the changing orbital radius as well as the inclination of the outer orbit and the position of the BBH in that orbit:

$$\Phi_{D,src}(f_{GW}) = 2\pi f_{GW}\frac{a_o(1 - e_o^2)\sin\iota_J}{1 + e_o\cos(\varphi(t))}\sin(\varphi(t) + \gamma_o) \tag{24}$$

.

C. Neglected Orbital Dynamics

We consider the implications of non-zero BH spins on the orbital dynamics. The precession of $\hat{L}_o$ around the spin of the SMBH $\hat{S}_3$ with $S_3 = \chi_3 M_3^2$ has characteristic frequency [16]

$$\Omega_{L_o, S_3} = \frac{S_3(4 + 3(M_1 + M_2)/M_3)}{2a_o^3(1 - e_o^2)^{3/2}}. \tag{25}$$

With $M_3 = 10^8 M_\odot \gg M_1 + M_2$, $a_o/M_3 = 100$ (or $a_o \sim 100$ AU), and $e_o = 0.3$, the characteristic time scale for this precession is $t_{L_o, S_3} = 1/\Omega_{L_o, S_3} \sim 7/\chi_3$ years. Even for rapidly spinning SMBHs, this effect is about one order of magnitude slower than de Sitter precession, so for now, we neglect it. It is worth noting that each successive effect included in the waveform modulation generally increases the magnitude of Fisher matrix terms. As such, we expect that future inclusion of this effect will lead to further improved parameter estimation uncertainties.

Lense-Thirring precession of $\hat{L}_i$ around $\hat{S}_3$ also contributes to the orbital dynamics, with

$$\Omega_{L_i, S_3} = \frac{S_3}{2a_o^3(1 - e_o^2)^{3/2}}. \tag{26}$$

This precession frequency is one-quarter of Ω_{L_o, S_3}, and thus, since we treat Ω_{L_o, S_3} as small in this work, we do the same for Ω_{L_i, S_3}.

We also consider Lidov-Kozai oscillations, the exchange between outer orbit eccentricity and inclination between $\hat{L}_o$ and $\hat{L}_i$. These oscillations have a characteristic frequency of [16]

$$\Omega_{LK} = \Omega_i \frac{M_3}{M_1 + M_2}\left(\frac{a_i}{a_o\sqrt{1 - e_o^2}}\right)^3, \tag{27}$$

where $\Omega_i = \sqrt{(M_1 + M_2)/a_i^3}$. Noting that $f_{GW} = \omega_{GW}/2\pi = \Omega_i/\pi$, we find that for $M_3 = 10^8 M_\odot \gg M_1 + M_2$, $a_o/M_3 = 100$, and $e_o = 0.3$, $t_{LK} \sim 2.2 \times 10^4 f_{GW}^2$ years. In our frequency band of interest, this effect occurs over much longer time scales than the de Sitter precession, and since both de Sitter precession and Lidov-Kozai oscillations modulate L_i, we neglect the slower of the two processes.

We furthermore assume that the eccentricity of the inner binary e_i is zero. As explained in [10], the inner eccentricity does not affect any component of the measured strain outside of the carrier waveform $\tilde{h}_C(f_{GW})$,

and thus should influence parameter estimation uncertainties primarily through the SNR. A higher e_i leads to faster merger times; however, high eccentricity BBHs can still remain in the millihertz and decihertz frequency bands throughout the entire observation period with just a larger initial separation between the two stellar mass BHs. So, it is expected that even as e_i approaches 1, such BBHs will offer long enough integration times to generate a moderate SNR, and therefore the inner eccentricity should not significantly alter the results of the simplified Fisher matrix analysis (see [10] for a more detailed discussion).

At this time, we neglect the effect of the precession of the outer orbit pericenter on the waveform. However, we can expect that such precession has a significant effect on the Doppler phase shift during the observation window, as the secular precession frequency is twice that of de Sitter precession [17]. A future work will explore the effect of pericenter precession on the parameter estimation uncertainties.

III. SIMPLIFICATIONS TO THE FISHER MATRIX APPROACH

In this analysis, we implement the Fisher information matrix method (as done in [10]) as a simple estimator for how well properties of a BBH+SMBH triple system can be measured. We make a number of well-supported assumptions to reduce the complexity of the numerical methods used to estimate parameter uncertainties.

A. Parameter Uncertainties from the Fisher Information Matrix

We first outline how the Fisher information matrix (or Fisher matrix) is used to estimate parameter measurement uncertainties. The elements of the Fisher matrix are defined as

$$\Gamma_{ab} \equiv \left(\frac{\partial \tilde{h}(f)}{\partial \theta_a} \Big| \frac{\partial \tilde{h}(f)}{\partial \theta_b} \right), \tag{28}$$

where

$$\left(\tilde{g} | \tilde{h} \right) = 4 \operatorname{Re} \int_0^\infty \frac{\tilde{g}^*(f)\tilde{h}(f)}{S_n(f)} df, \tag{29}$$

$\tilde{h}$ is the frequency-domain waveform, $S_n(f)$ is the PSD of the detector noise, and θ_a are the various parameters of the system.

We note that we use a finite difference method to compute $\partial \tilde{h}/\partial \theta_a$. To choose a finite parameter difference $\Delta \theta_a$ from which to estimate $\partial \tilde{h}/\partial \theta_a$, we minimize the quantity ϵ, analogous to waveform mismatch,

$$\epsilon = 1 - \frac{(\partial_{[\Delta\theta_a]}\tilde{h} | \partial_{[4\Delta\theta_a]}\tilde{h})}{\sqrt{(\partial_{[\Delta\theta_a]}\tilde{h} | \partial_{[\Delta\theta_a]}\tilde{h})(\partial_{[4\Delta\theta_a]}\tilde{h} | \partial_{[4\Delta\theta_a]}\tilde{h})}}, \tag{30}$$

where

$$\partial_{[\Delta\theta]}\tilde{h} = \frac{\tilde{h}(\theta + \Delta\theta) - \tilde{h}(\theta - \Delta\theta)}{2\Delta\theta}. \tag{31}$$

Minimizing this quantity gives us the best accuracy in computing the numerical derivative, as ϵ begins to increase once $\Delta \theta_a$ becomes so small that the changes in $\tilde{h}$ are smaller than computer precision. The choice of $4\Delta\theta_a$ to compare to $\Delta\theta_a$ is arbitrary.

The Fisher information matrix is related to the covariance matrix roughly by

$$\Sigma_{ab} = [\Gamma^{-1}]_{ab} + \mathcal{O}(\rho^{-4}), \tag{32}$$

where ρ is the signal-to-noise ratio (SNR). So, in the limit of large SNR, the covariance between two parameters $\Delta\theta_i \Delta\theta^j$ is approximately equal to the corresponding element of the inverse of the Fisher information matrix. As such, the parameter estimation uncertainty is given by $\Delta\theta_i = (\Sigma_{ii})^{0.5}$. If a network of GW detectors were to observe the same system, the Fisher information matrix would scale as the sum of the matrix elements for each detector, or

$$(\Gamma_{ab})^{\text{network}} = \sum_{det} \Gamma_{ab}^{det}. \tag{33}$$

This also applies to an observatory like LISA, whose three arms compose two interferometric detectors.

B. Reduced Fisher Matrix Dimensions

We can further reduce the dimensions of the Fisher matrix by removing certain physical parameters from the analysis. Doing so reduces the time it takes both to compute the complete Fisher matrix and invert it to find the covariance matrix and serves to reduce the condition number, leading to improved numerical accuracy in the inversion [13]. Since we have chosen to neglect all spin-precessional effects, the spin magnitudes and directions for each of the three black holes in the system are removed from the waveform and thus not included in the Fisher matrix.

Furthermore, we assume that space-based detectors like LISA or TianGO will act in conjunction with ground-based observatories, which are far more sensitive to the chirp mass $\mathcal{M}$, the mass ratio q, and the time and phase of coalescence t_c and ϕ_c [7]. So, knowing that a network of ground-based detectors can measure these quantities with much better precision than space-based observatories, we treat these four parameters as perfectly known in our analysis.

Finally, computation of the Fisher matrix with the remaining 12 parameters shows that for the average system in our parameter space of triple system properties, the uncertainties derived from the covariance matrix for $\log d_L$, $\overline{\theta}_S$, $\overline{\phi}_S$, $\overline{\theta}_J$, $\overline{\phi}_J$, λ_L, α_0, and $\log M_3$ fall in the range of $\sim 10^{-1} - 10^{-3}$, while those for $\Omega_o = \sqrt{M_3/a_o^3}$,
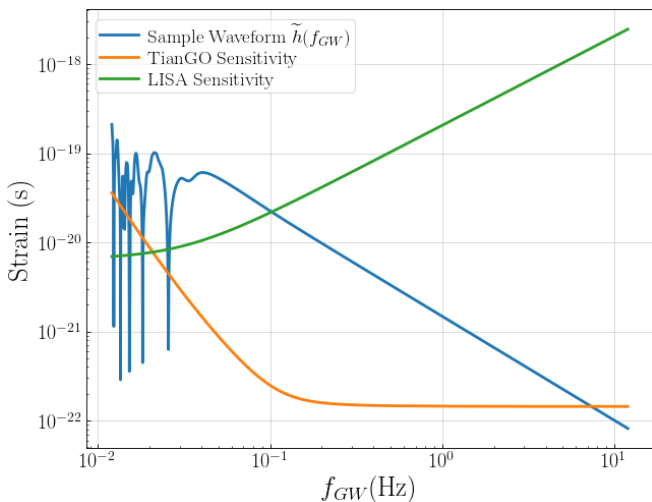
FIG. 2. An example waveform $\tilde{h}(f_{GW})$ with $M_3 = 10^8 M_\odot$, $a_o = 100 M_3$, and $e_o = 0.3$, along with approximate sensitivity curves for TianGO and LISA used in the Fisher matrix calculations done in this work.

e_o, γ_o, and ϕ_o roughly lie between a few $\times 10^{-7}$ and a few $\times 10^{-6}$. The small uncertainties in these parameters originate in the large modulation depth of the Doppler shift With uncertainties approaching three orders of magnitude improved over the other parameters, we can also treat the four parameters Ω_o, e_o, γ_o, and ϕ_o as perfectly known when investigating uncertainties in the remaining eight. Of course, when calculating parameter estimation uncertainties for any of the excluded parameters, they must be temporarily reincluded in the Fisher matrix.

IV. RESULTS AND DISCUSSION

We examine a BBH+SMBH triple system with fixed parameters $M_1 = M_2 = 50 M_\odot$, $t_c = 0$, $\phi_c = 0$, $D_L = 1\text{Gpc}$, $(\bar{\theta}_S, \bar{\phi}_S) = (33°, 147°)$, $(\bar{\theta}_J, \bar{\phi}_J) = (75°, 150°)$, and $\lambda_L = 45°$. For both LISA and TianGO, we compute the Fisher matrix where the integration is taken over a frequency window corresponding to an observation time of five years and the highest frequency is $f_{max} = 12$ Hz – this roughly corresponds to a lowest frequency of $f_{min} \sim 12$ mHz. In Figure 2, we plot an example frequency-domain waveform along with the TianGO and LISA sensitivity curves used in computing Fisher matrix elements.

The choice to use the same observation frequency band for both TianGO and LISA, which have sensitivities targeted towards different GW frequency bands, merits some explanation. The frequency band chosen roughly aligns with the most sensitive region of TianGO, but this is not the case for LISA. Figure **??** below shows the measurement uncertainty $\Delta(\log M_3) = \Delta M_3/M_3$, for $M_3 = 10^8 M_\odot$, $a_o/M_3 = 100$, and $e_o = 0.3$ as the ending GW frequency for the five-year LISA observation win-

dow is varied. For frequencies f_{end} above $\sim 10^{-2}$ Hz, the measurement uncertainty stays nearly constant. We attribute this to the following: since the time-frequency relation roughly follows $t(f_{GW}) \propto f_{GW}^{-8/3}$, increasing f_{end} adds frequency space for integration over at the upper bound and removes much less frequency space at the lower end. However, the additional frequency space added at the upper bound suffers from greater $S_n(f)$, and thus contributes very weakly to the Fisher matrix integrals. So, the Fisher matrix elements stay nearly constant. However, when the ending observation frequency is chosen to be significantly lower, the same time-frequency relation greatly reduces the width of the frequency range encompassed by the five-year observation window. The Fisher matrix elements thus decrease in magnitude, leading to poorer measurement uncertainties. We can see that an ending frequency of 12 Hz is appropriate for estimating the levels of parameter measurement precision that can be obtained by both LISA and TianGO.

In Figure 3, we plot the fractional uncertainty in the SMBH mass M_3, measured by TianGO, as we vary M_3 and a_o. At each point, we sample the covariance found with the Fisher matrix over combinations of the three geometrical phases – that is, 6 choices of both γ_o and ϕ_o and 12 choices of α_0, or 432 sets of $(\gamma_o, \alpha_0, \phi_o)$ – and find the median. The purple regions denote where the outer binary merges in less than the proposed observation length of five years. We expect systems in this region to be exceedingly rare, as there is only a short window for such systems to form in order to be detected by TianGO. The gray region corresponds to where the measurement uncertainty $\Delta \lambda_L$, also determined via the Fisher matrix, exceeds λ_L. In other words, the value $\lambda_L = 0$ is not excluded from the confidence interval, and since de Sitter precession does not occur when $\lambda_L = 0$, the signal of precession is not absolutely detectable. We set the criterion that if two-thirds of the sampled $(\gamma_o, \alpha_0, \phi_o)$ triplets for a given $(M_3, a_o/M_3)$ result in $\Delta \lambda_L > \lambda_L$, that particular $(M_3, a_o/M_3)$ pair is placed in the gray region. Figure 4 gives the same results, but using the LISA detector response and noise curve instead of that of TianGO.

We note that the fractional uncertainty in the outer orbit semimajor axis $\Delta a_o/a_o$ should follow a similar pattern. Using the chain rule and $a_o^3 = M_3/\Omega_o^2$, we find

$$3\frac{a_o^3}{M_3}\frac{\Delta a_o}{a_o} = \frac{1}{\Omega_o^2}\frac{\Delta M_3}{M_3} - 2\frac{1}{\Omega_o^2}\frac{\Delta \Omega_o}{\Omega_o}, \qquad (34)$$

and recalling that $\Delta \Omega_o/\Omega_o$ is very small compared to $\Delta M_3/M_3$,

$$\frac{\Delta a_o}{a_o} \approx \frac{1}{3}\frac{\Delta M_3}{M_3}. \qquad (35)$$

We observe that TianGO has the potential to realize fractional uncertainties significantly below the 0.1% level across a wide range of parameters of the triple system

and that LISA could possibly reach similar thresholds. The contour plots also demonstrate the importance of de Sitter precession in the measurability of M_3 and a_o. We see that broadly across the $(M_3, a_o/M_3)$ parameter space explored, equal fractional uncertainties roughly follow lines of constant P_{dS}. More rapid de Sitter precession of $\hat{L}_i$ leads to greater total modulation of the BBH waveform over the observation time as the location of a detector shifts within the the evolving GW antenna pattern. Furthermore, for both LISA and TianGO, we see that regardless of the value of e_o, the boundary where the region with $\Delta\lambda_L > \lambda_L$ is separated from the region where precession is detectable roughly along the line of $P_{dS} = 10$ years, twice the observation run length.

We conduct an identical analysis for the estimation uncertainties in e_o by both TianGO and LISA, as shown in Figures 5 and 6. These results suggest that the eccentricity can be constrained to high precision, with TianGO able to achieve a lower bound of $\Delta e_o \sim 10^{-6} - 10^{-5}$ and LISA able to achieve $\Delta e_o \sim 10^{-5} - 10^{-4}$ across a substantial portion of the parameter space where precession is detectable. Once again, we see the importance of de Sitter precession in the measurability of this parameter, as across a sizeable portion of the parameter space, equivalent estimation uncertainties match contours of equal de Sitter precession period. Closer to the $\Delta\lambda_L > \lambda_L$ boundary, lines of equal estimation uncertainty roughly follow lines of constant $M_3 a_o^3$.

An important question is the impact of increasing eccentricity on the ability to measure parameters like M_3, a_o, and e_o itself. In Figures 7 and 8, we study the effect of increasing eccentricity on the estimation uncertainties in M_3 and e_o (recalling again that $\Delta a_o/a_o \approx \frac{1}{3}\Delta M_3/M_3$). We see that as the eccentricity increases, we can attain marginal improvements in the measurement of M_3 and e_o – a factor of $\sim$ a few – though this improvement is not universal across $(M_3, a_o/M_3)$ parameter space. We attribute this improvement to a combination of two factors.

First, as seen in Equation 6, an increasing eccentricity leads to faster de Sitter precession. This leads to more rapid evolution of the orientation of the BBH's radiation angular pattern relative to GW observatories, and thus more rapid modulation of the GW signal. Figures 7 and 8 show that improvement in parameter estimation uncertainties is most pronounced when the de Sitter precession period is already short compared to the five-year observation run duration. We conclude that when the inner angular momentum $\hat{L}_i$ completes only a few precessional cycles during the observation run, a decrease in the precessional period is rather insignificant in parameter estimation, but as the system completes more cycles during the five years, a similar decrease in the period induces a more noticeable change in measurement uncertainties. This may be associated with driving more GW waveform modulation at frequencies closer to the merger event, where the signal is typically strongest.

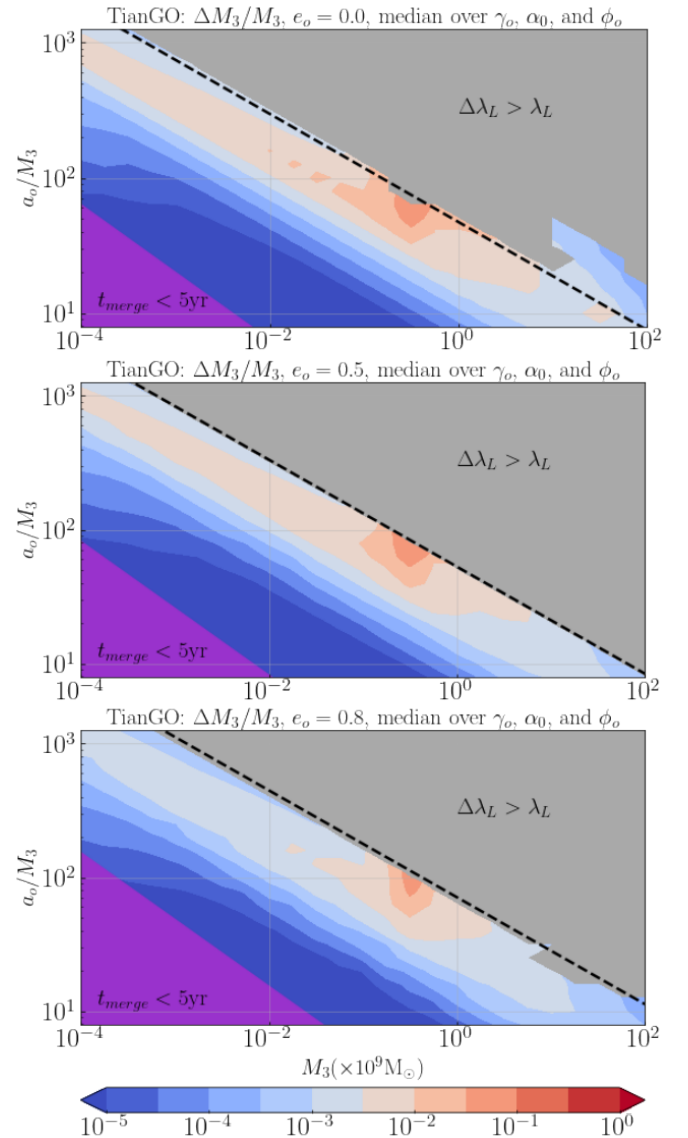Second, an increasing eccentricity further deforms the

FIG. 3. Fractional uncertainty in M_3 as measured by TianGO for three different eccentricities $e_o = \{0, 0.5, 0.8\}$. At each point in the contour plot, we take the median uncertainty over a set of 432 combinations of $(\gamma_o, \alpha_0, \phi_o)$. The purple region corresponds to where the outer binary merges in less time than the observation duration, and the gray region corresponds to where precession is not detectable (i.e., $\lambda_L = 0$ cannot be ruled out of the parameter estimation confidence interval). The dashed line corresponds to $P_{dS} = 10$ yr, twice the observation run length.

shape of the outer orbit, extending the range of Doppler phase shift modulation for certain values of γ_o. However, this effect is secondary in nature when averaging over outer orbit angular parameters, as for some values of γ_o, an increased eccentricity actually reduces the Doppler phase shift range, as the Doppler phase shift depends on the line of sight distance of the BBH from the SMBH and certain orientations of the elliptic orbit lead to reduced line of sight distance variation.
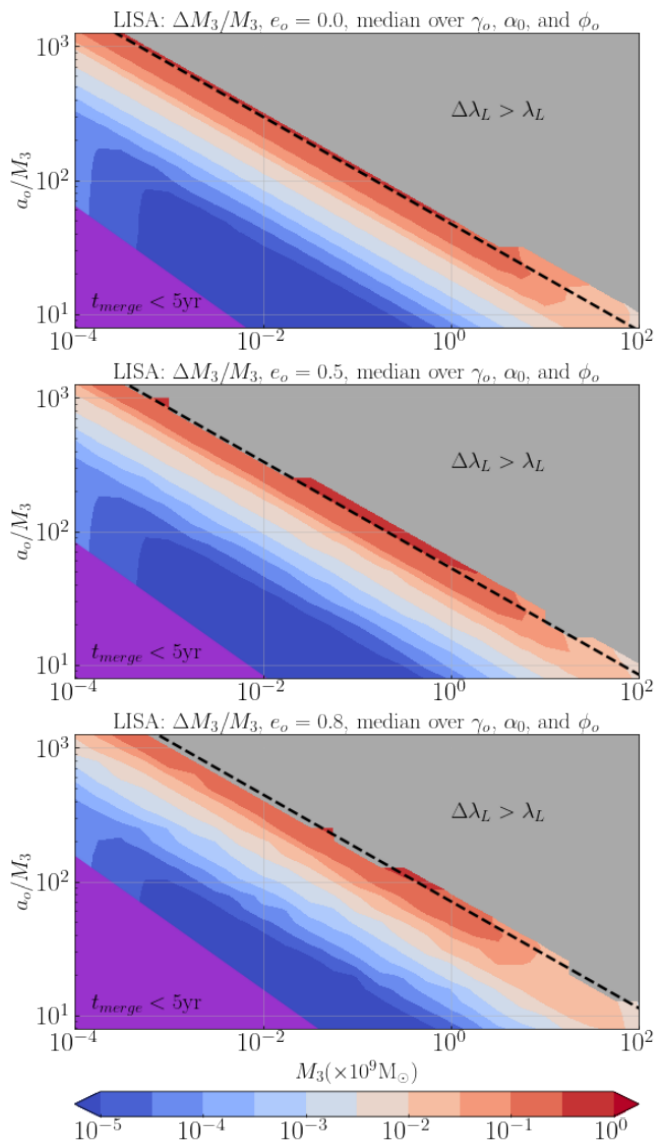
FIG. 4. Same as Figure 3, but measured by LISA instead.

FIG. 5. Uncertainty in e_o as measured by TianGO for three different eccentricities $e_o = \{0, 0.5, 0.8\}$. The same sampling procedure as used in Figure 3 and 4 is applied here, as are the method for excluding regions. Slight changes in the shape of the region where $\Delta\lambda_L > \lambda_L$ as compared to Figure 3 result from the reinclusion of e_o into the Fisher matrix, which is necessary to calculate Δe_o.

We finally consider the relative abilities of TianGO and LISA in measuring parameters of BBH+SMBH triples. Figures 9 and 10 give the ratios of measurement uncertainties attainable by TianGO to those attainable by LISA as we vary the eccentricity and move through $(M_3, a_o/M_3)$ parameter space. Across a substantial portion of the parameter space, the measurement uncertainties attainable by the two detectors are quite comparable, falling within less than a factor of two of one another. This portion lies closer to the region where $t_{merge} < 5$ years, so we expect that triple systems where the performance of LISA will be comparable to TianGO will generally be more uncommon. However, as we approach the line of a ten-year de Sitter precession period (roughly marking where the signal of de Sitter precession becomes detectable), the advantage of TianGO is apparent, as this detector can attain uncertainties improved over LISA by
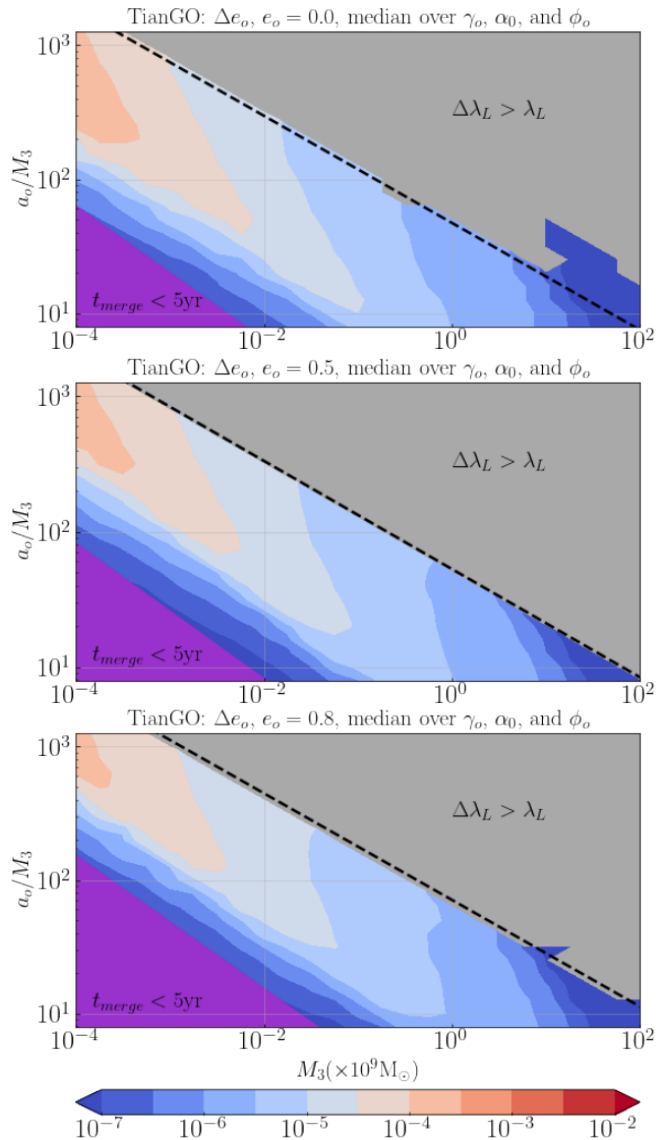
an order of magnitude or more. This result marks an important benefit of a dedicated decihertz GW detector: the properties of BBH+SMBH triple systems which have only a weak signal of de Sitter precession can be precisely constrained by a decihertz detector like TianGO or B-DECIGO, which have frequency bands that are better aligned to where the SMBH-induced GW modulation occurs than those of millihertz GW detector concepts.
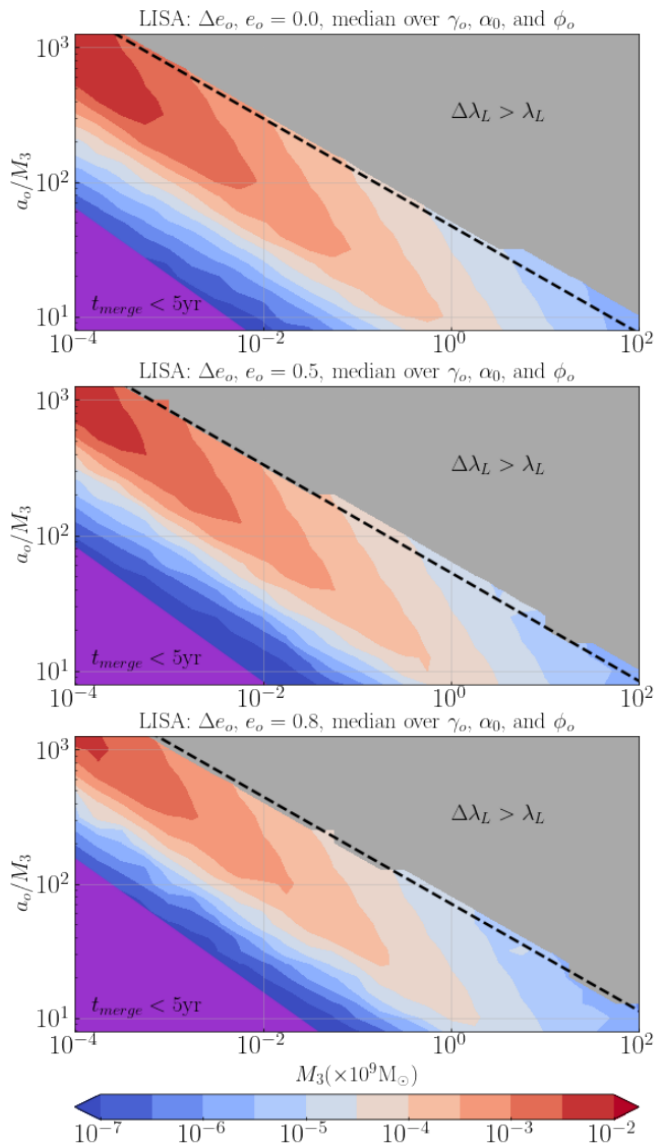
FIG. 6. Same as Figure 5, but measured by LISA instead.

V. CONCLUSION AND FUTURE DIRECTIONS

Using the Fisher information matrix, we have shown that future space-based GW observatories may be able to precisely constrain the properties of BBH+SMBH triple systems, like the SMBH mass and outer orbit semimajor axis and eccentricity, through the GW signal observed from the BBH. We have demonstrated that the rate of de Sitter precession is an important determinant in the measurability of triple system parameters and that an increasing outer orbit eccentricity leads to improved measurement uncertainties through greater Doppler phase shift modulation and faster de Sitter precession. We have also shown that the planned LISA detector is capable of measuring these systems, though decihertz detector concepts such as TianGO or B-DECIGO possess a competitive advantage over LISA in measuring such quantities,
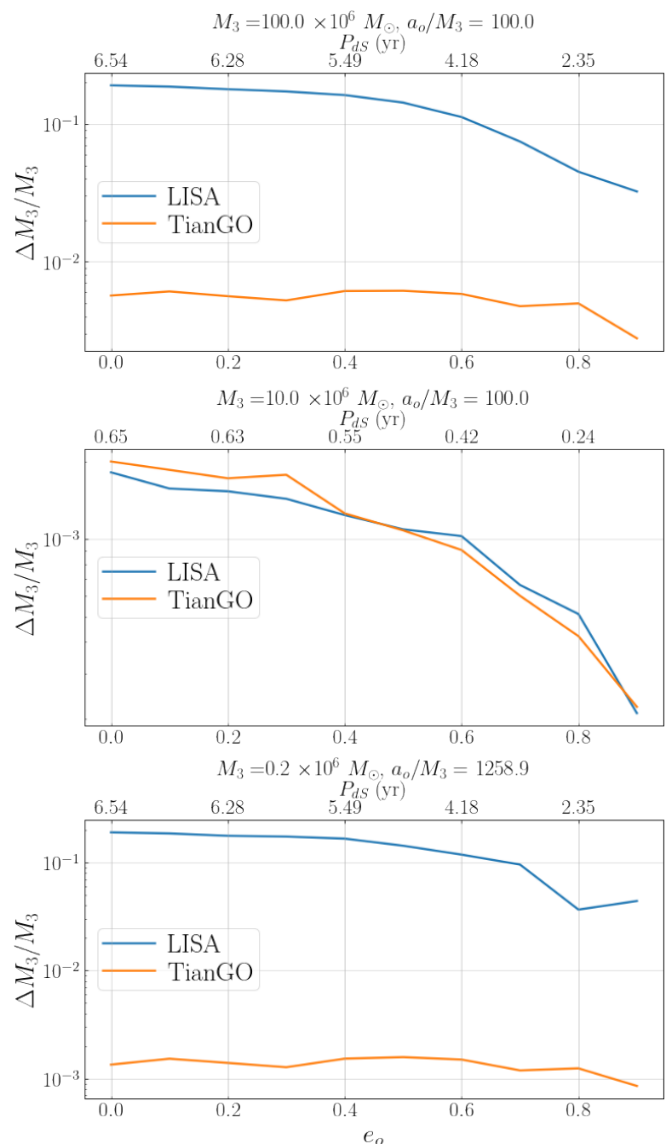

FIG. 7. The fractional uncertainties in M_3 obtainable by TianGO vs LISA for three choices of $(M_3, a_o/M_3)$ as the eccentricity is varied. At point where the de Sitter precession is slower, TianGO can significantly outperform LISA. As the de Sitter precession becomes faster, the two detectors attain more comparable performance.

especially in triple systems which have only a weak signal of de Sitter precession.

There are some important limitations of the Fisher information method implemented in this work. As described in [13], the inverse Fisher matrix gives the covariance of the posterior probability distribution for the true source parameters θ_0 for a single experiment under a few conditions: the noise is Gaussian, the prior probability distributions are roughly constant in the local region of θ_0 in parameter space, and the SNR is high. For typical parameters in the ranges we explore in this work, the SNR of the waves from the stellar mass binary gener-
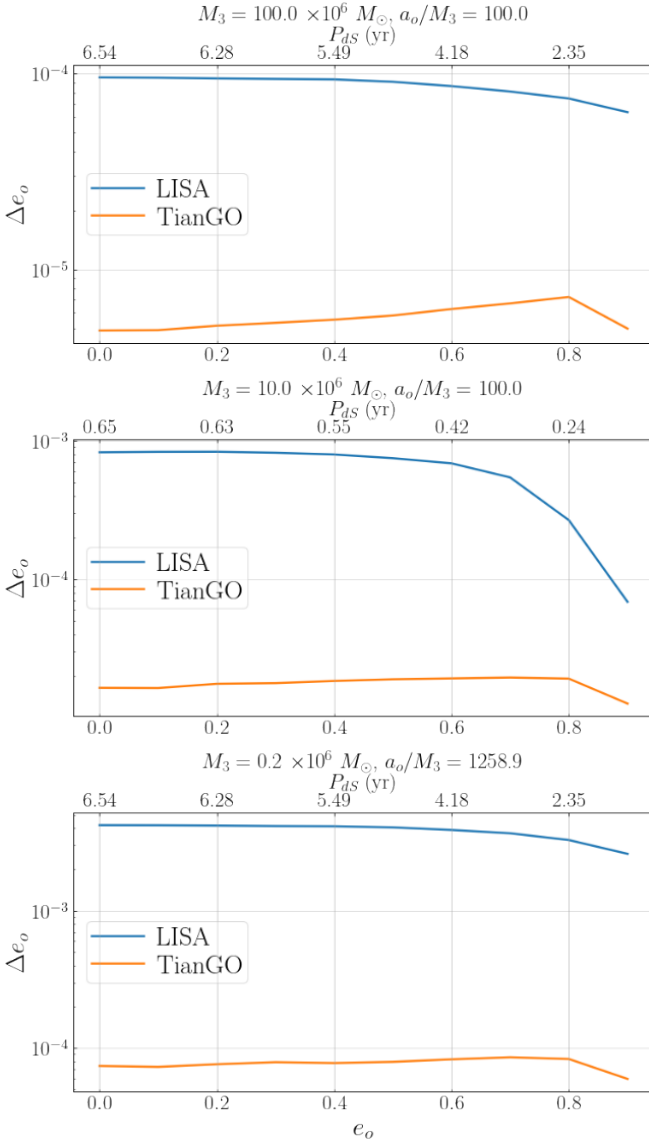
FIG. 8. Same as Figure 7, but estimating the outer eccentricity variance Δe_o. TianGO tends to significantly outperform LISA across a much wider range of $(M_3, a_o/M_3)$ than in the $\Delta M_3/M_3$ case.

FIG. 9. The ratio of the fractional uncertainties in M_3 obtainable by TianGO as opposed to LISA for three different choices in eccentricity.

ally stays near 40 for TianGO, but is only ~ 4 for LISA. The lower SNR suggests that the true parameter estimation uncertainties may be significantly different than those calculated here. However, the inverse Fisher matrix is also equivalent to the Cramér-Rao bound, that is, the *lower bound* for the uncertainty of an unbiased estimator of θ_0 [13]. So, the Fisher matrix method employed here essentially offers a best-case scenario for the parameter estimation precision obtainable by future space-based observatories. A more thorough approach to this analysis will implement a full Bayesian methodology, but this work still serves as a meaningful stepping stone upon which future calculations can be built.

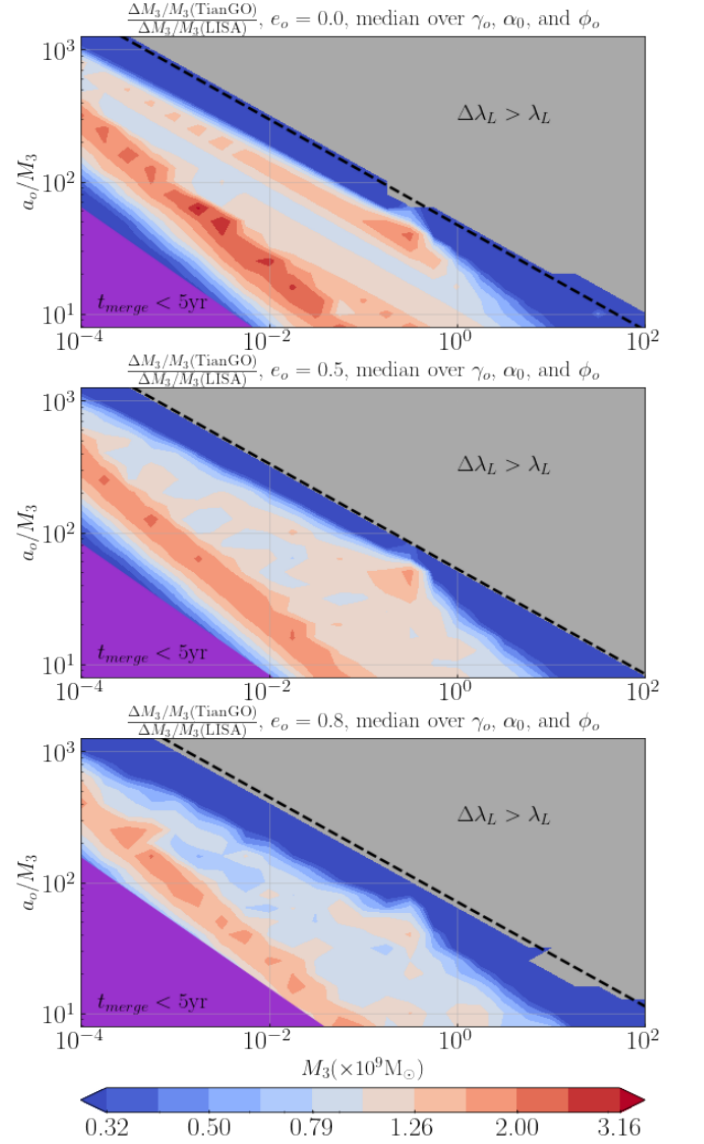We can further develop this work by inclusion of ad-

ditional effects into the waveform. One of the next order effects is the precession of the outer orbit pericenter, which, as a secular average, follows

$$\dot\gamma_o = 3\frac{M_3}{a_o(1-e_o^2)}\Omega_o. \tag{36}$$

[17]. Additionally, for triple systems with lower outer binary merger times (i.e., with M_3 and a_o/M_3 near the purple regions shown in Figures 3, 4, 5, and 6), the semi-major axis and outer eccentricity can evolve significantly in time due to radiation reaction. These time derivatives
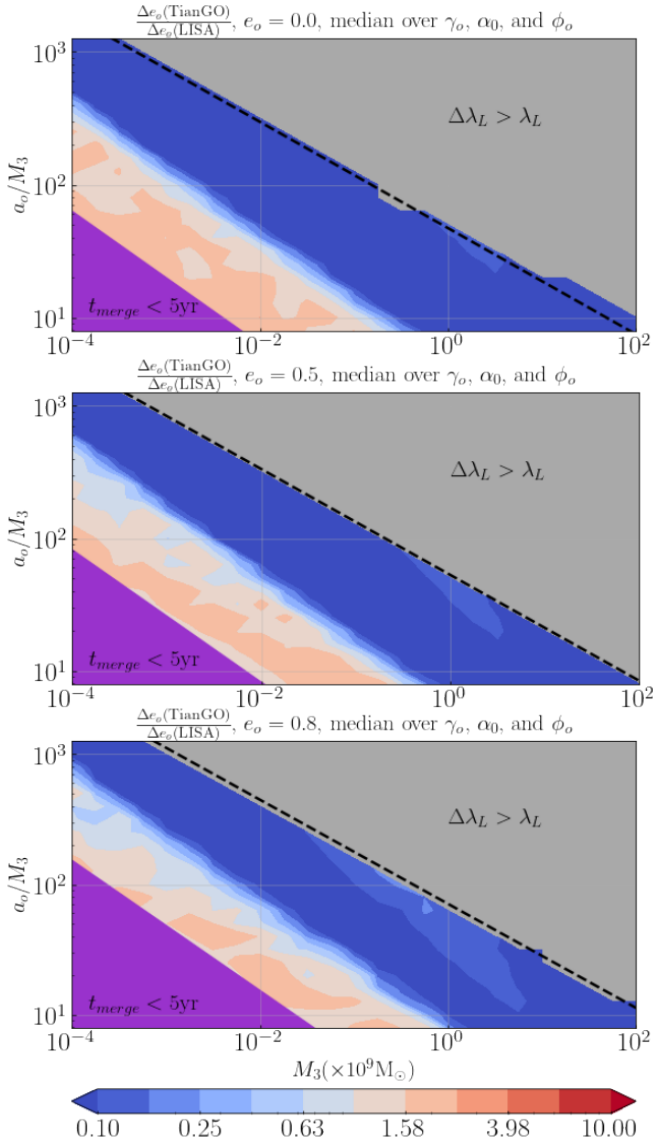
FIG. 10. The ratio of the uncertainties in e_o obtainable by TianGO as opposed to LISA for three different choices in eccentricity.

observatory, even in the case of a circular outer orbit. It would be interesting to examine the combined effects of an eccentric outer orbit and repeated GW lensing in parameter estimation problems.

follow

$$\dot{a}_o = -\frac{64}{5}\frac{G^3\mu M_{tot}^2}{c^5 a_o^3}\frac{1}{(1-e_o^2)^{7/2}}\left(1+\frac{73}{24}e_o^2+\frac{37}{96}e_o^4\right) \quad (37)$$

$$\dot{e}_o = -\frac{304}{15}\frac{G^3\mu M_{tot}^2}{c^5 a_o^4}\frac{e_o}{(1-e_o)^{5/2}}\left(1+\frac{121}{304}e_o^2\right), \quad (38)$$

where $M_{tot} = M_1 + M_2 + M_3$ and $\mu = \frac{(M_1+M_2)M_3}{M_{tot}}$ [8]. Furthermore, we can consider including the spin-precession effects that we chose to neglect in II C due to their significantly slower time scales.

Finally, in Ref. [18], it is discussed how gravitational lensing of GWs by the SMBH combined with the de Sitter precession of $\boldsymbol{L}_i$ can further constrain the parameters of a triple system as estimated by a space-based GW

[1] B. P. Abbott *et al.* (LIGO Scientific, Virgo), GWTC-1: A Gravitational-Wave Transient Catalog of Compact Binary Mergers Observed by LIGO and Virgo during the First and Second Observing Runs, Phys. Rev. X **9**, 031040 (2019), arXiv:1811.12907 [astro-ph.HE].

[2] R. Abbott *et al.* (LIGO Scientific, Virgo), GWTC-2: Compact Binary Coalescences Observed by LIGO and Virgo During the First Half of the Third Observing Run, Phys. Rev. X **11**, 021053 (2021), arXiv:2010.14527 [gr-qc].

[3] B. P. Abbott *et al.* (LIGO Scientific, Virgo), Observation of Gravitational Waves from a Binary Black Hole Merger, Phys. Rev. Lett. **116**, 061102 (2016), arXiv:1602.03837 [gr-qc].

[4] P. Amaro-Seoane *et al.* (LISA), Laser Interferometer Space Antenna, (2017), arXiv:1702.00786 [astro-ph.IM].

[5] S. Kawamura *et al.*, Current status of space gravitational wave antenna DECIGO and BDECIGO (2020), arXiv:2006.13545 [gr-qc].

[6] K. A. Kuns, *Future Networks of Gravitational Wave Detectors: Quantum Noise and Space Detectors*, Ph.D. thesis, University of California, Santa Barbara (2019).

[7] K. A. Kuns, H. Yu, Y. Chen, and R. X. Adhikari, Astrophysics and cosmology with a decihertz gravitational-wave detector: TianGO, Phys. Rev. D **102**, 043001 (2020), arXiv:1908.06004 [gr-qc].

[8] M. Maggiore, *Gravitational Waves. Vol. 1: Theory and Experiments*, Oxford Master Series in Physics (Oxford University Press, 2007).

[9] T. A. Apostolatos, C. Cutler, G. J. Sussman, and K. S. Thorne, Spin induced orbital precession and its modulation of the gravitational wave forms from merging bina-ries, Phys. Rev. D **49**, 6274 (1994).

[10] H. Yu and Y. Chen, Direct determination of supermassive black hole properties with gravitational-wave radiation from surrounding stellar-mass black hole binaries, Phys. Rev. Lett. **126**, 021101 (2021), arXiv:2009.02579 [gr-qc].

[11] B.M. Peterson, Measuring the Masses of Supermassive Black Holes, Space Sci. Rev. **183** (2014).

[12] D. C. Heggie, Binary evolution in stellar dynamics, Mon. Not. Roy. Astron. Soc. **173**, 729 (1975).

[13] M. Vallisneri, Use and abuse of the Fisher information matrix in the assessment of gravitational-wave parameter-estimation prospects, Phys. Rev. D **77**, 042001 (2008), arXiv:gr-qc/0703086.

[14] E. Poisson and C. M. Will, *Gravity: Newtonian, Post-Newtonian, Relativistic* (Cambridge Univ. Press, 2014).

[15] S. Droz, D. J. Knapp, E. Poisson, and B. J. Owen, Gravitational waves from inspiraling compact binaries: Validity of the stationary phase approximation to the Fourier transform, Phys. Rev. D **59**, 124016 (1999), arXiv:gr-qc/9901076.

[16] B. Liu and D. Lai, Probing the Spins of Supermassive Black Holes with Gravitational Waves from Surrounding Compact Binaries, Astrophys. J. **924**, 127 (2022), arXiv:2105.02230 [astro-ph.HE].

[17] R. S. Park, W. M. Folkner, A. S. Konopliv, J. G. Williams, D. E. Smith, and M. T. Zuber, Precession of mercury's perihelion from ranging to themessengerspace-craft, The Astronomical Journal **153**, 121 (2017).

[18] H. Yu, Y. Wang, B. Seymour, and Y. Chen, Detecting gravitational lensing in hierarchical triples in galactic nuclei with space-borne gravitational-wave observatories, Phys. Rev. D **104**, 103011 (2021), arXiv:2107.14318 [gr-qc].